

**Multi-angle fluorometer technique for the determination of absorption and scattering coefficients of subwavelength nanoparticles**

Author

Shortell, Matthew P, Hewins, Rodney A, Fernando, Joseph FS, Walden, Sarah L, Waclawik, Eric R, Jaatinen, Esa A

Published

2016

Journal Title

Optics Express

Version

Version of Record (VoR)

DOI

[10.1364/oe.24.017090](https://doi.org/10.1364/oe.24.017090)

Rights statement

Published by The Optical Society under the terms of the Creative Commons Attribution 4.0 License. Further distribution of this work must maintain attribution to the author(s) and the published article's title, journal citation, and DOI.

Downloaded from

<https://hdl.handle.net/10072/430245>

Griffith Research Online

<https://research-repository.griffith.edu.au>

# Multi-angle fluorometer technique for the determination of absorption and scattering coefficients of subwavelength nanoparticles

MATTHEW P. SHORTELL,\* RODNEY A. HEWINS, JOSEPH F. S. FERNANDO, SARAH L. WALDEN, ERIC R. WACLAWIK AND ESA A. JAATINEN

*School of Chemistry, Physics and Mechanical Engineering, Science and Engineering Faculty, Queensland University of Technology (QUT), Brisbane, Queensland, 4000, Australia*

\*[matthew.shortell@qut.edu.au](mailto:matthew.shortell@qut.edu.au)

**Abstract:** A thorough analysis of the resonance light scattering (RLS) technique for quantitative scattering measurements of subwavelength nanoparticles is reported. The systematic error associated with using a measurement at a single angle to represent all of the scattered light is investigated. In-depth analysis of the reference material was performed to identify and minimize the error associated with the reference material. Semiconductor ZnO nanobullets and spherical Au nanoparticles of various sizes were used to verify the approach. A simple and inexpensive modification to standard fluorometers is demonstrated using a glass prism allowing scattering measurements in the slightly forward and backwards directions. This allows quantification of the systematic error associated with RLS which is consistently overlooked.

Published by The Optical Society under the terms of the [Creative Commons Attribution 4.0 License](https://creativecommons.org/licenses/by/4.0/). Further distribution of this work must maintain attribution to the author(s) and the published article's title, journal citation, and DOI.

**OCIS codes:** (290.5820) Scattering measurements; (290.4020) Mie theory; (160.4236) Nanomaterials.

## References and links

1. E. S. Arinze, B. Qiu, G. Nyirjesy, and S. M. Thon, "Plasmonic nanoparticle enhancement of solution-processed solar cells: practical limits and opportunities," *ACS Photonics* **3**(2), 158–173 (2016).
2. P. Albella, R. Alcaraz de la Osa, F. Moreno, and S. A. Maier, "Electric and magnetic field enhancement with ultralow heat radiation dielectric nanoantennas: considerations for surface-enhanced spectroscopies," *ACS Photonics* **1**(6), 524–529 (2014).
3. M. Caldarola, P. Albella, E. Cortés, M. Rahmani, T. Roschuk, G. Grinblat, R. F. Oulton, A. V. Bragas, and S. A. Maier, "Non-plasmonic nanoantennas for surface enhanced spectroscopies with ultra-low heat conversion," *Nat. Commun.* **6**, 7915 (2015).
4. O. Bibikova, A. Popov, A. Bykov, A. Prilepskii, M. Kinnunen, K. Kordas, V. Bogatyrev, N. Khlebtsov, S. Vainio, and V. Tuchin, "Optical properties of plasmon-resonant bare and silica-coated nanostars used for cell imaging," *J. Biomed. Opt.* **20**(7), 076017 (2015).
5. D. Jaque, C. Richard, B. Viana, K. Soga, X. Liu, and J. García Solé, "Inorganic nanoparticles for optical bioimaging," *Adv. Opt. Photonics* **8**(1), 1 (2016).
6. J. Du, L. Jiang, Q. Shao, X. Liu, R. S. Marks, J. Ma, and X. Chen, "Colorimetric detection of mercury ions based on plasmonic nanoparticles," *Small* **9**(9-10), 1467–1481 (2013).
7. J. Du, B. Zhu, and X. Chen, "Urine for plasmonic nanoparticle-based colorimetric detection of mercury ion," *Small* **9**(24), 4104–4111 (2013).
8. R. de la Rica and M. M. Stevens, "Plasmonic ELISA for the ultrasensitive detection of disease biomarkers with the naked eye," *Nat. Nanotechnol.* **7**(12), 821–824 (2012).
9. L. Polavarapu, J. Pérez-Juste, Q.-H. Xu, and L. M. Liz-Marzán, "Optical sensing of biological, chemical and ionic species through aggregation of plasmonic nanoparticles," *J. Mater. Chem. C Mater. Opt. Electron. Devices* **2**(36), 7460–7476 (2014).
10. G. Tian, W. Ren, L. Yan, S. Jian, Z. Gu, L. Zhou, S. Jin, W. Yin, S. Li, and Y. Zhao, "Red-emitting upconverting nanoparticles for photodynamic therapy in cancer cells under near-infrared excitation," *Small* **9**(11), 1929–1938 (2013).
11. C. Urban, C. Ayala, M. Shea, R. Schiff, N. Halas, and A. Joshi, "Reduction in nanoparticle size dramatically improves plasmonic photo-thermal therapy efficacy in aggressive triple negative breast cancer," in *Biomedical Optics Meeting* (2014), paper BW1B-1.
12. Q. Q. Dou, A. Rengaramchandran, S. T. Selvan, R. Paulmurugan, and Y. Zhang, "Core-shell upconversion nanoparticle - semiconductor heterostructures for photodynamic therapy," *Sci. Rep.* **5**, 8252 (2015).

13. S. Chaudhuri, S. Sardar, D. Bagchi, S. Dutta, S. Debnath, P. Saha, P. Lemmens, and S. K. Pal, "Photoinduced dynamics and toxicity of a cancer drug in proximity of inorganic nanoparticles under visible light," *ChemPhysChem* **17**(2), 270–277 (2016).
14. S. Sarina, E. R. Waclawik, and H. Zhu, "Photocatalysis on supported gold and silver nanoparticles under ultraviolet and visible light irradiation," *Green Chem.* **15**(7), 1814 (2013).
15. O. Ilic, I. Kaminer, Y. Lahini, H. Buljan, and M. Soljačić, "Exploiting optical asymmetry for controlled guiding of particles with light," *ACS Photonics* **3**(2), 197–202 (2016).
16. V. Weber, A. Feis, C. Gellini, R. Pilot, P. R. Salvi, and R. Signorini, "Far- and near-field properties of gold nanoshells studied by photoacoustic and surface-enhanced Raman spectroscopies," *Phys. Chem. Chem. Phys.* **17**(33), 21190–21197 (2015).
17. A. K. Gaigalas, L. Wang, V. Karpiak, Y.-Z. Zhang, and S. Choquette, "Measurement of scattering cross section with a spectrophotometer with an integrating sphere detector," *J. Res. Natl. Inst. Stand. Technol.* **117**, 202–215 (2012).
18. M. I. Cabrera, O. M. Alfano, and A. E. Cassano, "Absorption and scattering coefficients of titanium dioxide particulate suspensions in water," *J. Phys. Chem.* **100**(51), 20043–20050 (1996).
19. X. Zhang, A. Li, F. Liu, and X. Yan, "Measurement of localized surface plasmon resonance of metallic nanostructures," in *2015 Int. Conf. Mechatronics, Electron. Ind. Control Eng.* (2015), pp. 1502–1505.
20. C. Langhammer, B. Kasemo, and I. Zorić, "Absorption and scattering of light by Pt, Pd, Ag, and Au nanodisks: absolute cross sections and branching ratios," *J. Chem. Phys.* **126**(19), 194702 (2007).
21. W. Lu, B. S. Fernández Band, Y. Yu, Q. Geng Li, J. Chuan Shang, C. Wang, Y. Fang, R. Tian, L. Ping Zhou, L. Li Sun, Y. Tang, S. Hua Jing, W. Huang, and J. Ping Zhang, "Resonance light scattering and derived techniques in analytical chemistry: past, present, and future," *Mikrochim. Acta* **158**(1-2), 29–58 (2007).
22. R. F. Pasternack, C. Bustamante, P. J. Collings, A. Giannetto, and E. J. Gibbs, "Porphyrin assemblies on DNA as studied by a resonance light-scattering technique," *J. Am. Chem. Soc.* **115**(13), 5393–5399 (1993).
23. J. R. Lakowicz, *Principles of Fluorescence Spectroscopy* (Springer US, 2006).
24. J. R. G. Navarro and M. H. V. Werts, "Resonant light scattering spectroscopy of gold, silver and gold-silver alloy nanoparticles and optical detection in microfluidic channels," *Analyst (Lond.)* **138**(2), 583–592 (2013).
25. N. Xu, B. Bai, Q. Tan, and G. Jin, "Accurate geometric characterization of gold nanorod ensemble by an inverse extinction/scattering spectroscopic method," *Opt. Express* **21**(18), 21639–21650 (2013).
26. G. S. He, J. Zhu, K. T. Yong, A. Baev, H. X. Cai, R. Hu, Y. Cui, X. H. Zhang, and P. N. Prasad, "Scattering and absorption cross-section spectral measurements of gold nanorods in water," *J. Phys. Chem. C* **114**(7), 2853–2860 (2010).
27. C. F. Bohren and D. R. Huffman, eds., *Absorption and Scattering of Light by Small Particles* (Wiley-VCH Verlag GmbH, 1998).
28. J. F. S. Fernando, M. P. Shortell, C. J. Noble, J. R. Harmer, E. A. Jaatinen, and E. R. Waclawik, "Controlling Au photodeposition on large ZnO nanoparticles," *ACS Appl. Mater. Interfaces* **8**(22), 14271–14283 (2016).
29. F. Urbach, "The long-wavelength edge of photographic sensitivity and of the electronic absorption of solids," *Phys. Rev.* **92**(5), 1324 (1953).
30. J. F. S. Fernando, M. P. Shortell, K. C. Vernon, E. A. Jaatinen, and E. R. Waclawik, "Small gold nanoparticles as crystallization "catalysts": effect of seed size and concentration on Au-ZnO hetero nanoparticles," *Cryst. Growth Des.* **15**(9), 4324–4330 (2015).

## 1. Introduction

The extinction of light as it passes through a dispersion of nanoparticles (NPs) results from both absorption and scattering. Different applications require fast, effective and accurate quantification of absorption or scattering or both. In solution processed solar cells, scattering from plasmonic nanoparticles is used to increase the interaction length of light with the photovoltaic absorber and hence increase the efficiency of the solar cell [1]. However, absorption from the plasmonic nanoparticles usually results in heating rather than electron generation [2,3], so the ratio of absorption to scattering should be minimized for optimal solar cell efficiency [1]. Other processes that require high scattering cross-sections include in-vitro scattering microscopy [4,5] and molecule detection through the selective aggregation of plasmonic nanoparticles with target molecules [6–9].

In other applications maximizing the amount of absorption is important. For example in photodynamic therapy of cancer using semiconductor or Au nanoparticles, high light absorption in the infrared skin transmission window is important [10]. The absorption of light can generate sufficient heat to damage the cancer cells in the case of Au nanoparticles [11], or in the case of semiconductor nanoparticles, the exciton formed from absorption generates reactive oxygen species (ROS) or other chemical species that damage the cancerous tissue [12,13]. Similarly in photocatalysis [14] and optical manipulation of NP motion [15], controlling the amount of absorption is paramount for high conversion and manipulation efficiencies respectively.

Despite the clear importance of measuring the absorption and scattering components of extinction in a diverse range of applications, it is rarely performed and instead, absorption or scattering is simply inferred from extinction measurements. Measuring the extinction coefficient of NP dispersions is a relatively trivial task. UV-Vis spectrometers measure the transmission of light through a sample and the extinction coefficient is found using Beers' law. Separating the extinction into absorption and scattering is much more difficult. Several methods have been developed for this purpose. Photoacoustic methods measure absorption by measuring the change in pressure induced from heating through absorption of light [16]. Unfortunately, this technique is slow and relatively complicated. Integrating sphere methods provide a more direct technique for the measurement of absorption. Although the technique has been developed for absorption measurements of microparticles [17,18] and thin films [19,20], this technique has not been adequately developed for nanoparticle dispersions.

In the early 90s, a technique to measure the scattered light from large organic chromophores, known as Resonance Light Scattering (RLS), was proposed by Pasterneck et al. [21,22] to measure scattering in the spectral region near the strong absorption resonance of chromophores. It is a technique that is easy to implement and can be performed with a conventional fluorescence spectrophotometer (fluorometer). The method works by measuring emission from the sample at the same wavelength as the excitation but collected at 90° to the incident beam direction.

Since then, various adaptations were suggested to make the RLS technique quantitative to allow the separation of absorption and scattering. These include reducing the inner filter effect by taking scattering measurements at dilute concentrations [23,24] and removing wavelength variability in source and detector efficiency through the use of a suitable reference material (usually colloidal silica) [24,25]. Unfortunately, there has been a lack of consistency with the implementation of the technique applied to NPs. Furthermore, the variability of the scattering angular distribution with larger particles has not been adequately addressed, a problem that also plagues the integrating sphere technique [26].

In this paper, we propose a simple method to perform RLS measurements in a conventional fluorometer at angles other than 90° using a Littrow prism to redirect the scattered light. This allows comparison measurements to be performed to confirm the accuracy of the 90° scattering measurement. We also clearly outline the requirements and methods for quantitative RLS measurements to remove any ambiguity from the literature on how to perform scattering measurements to separate absorption and scattering from extinction coefficients in nanoparticle dispersions.

## 2. Scattering measurements methodology

### 2.1 Introduction to scattering measurements

The transmission of light through a slab of material of thickness  $L$  and extinction coefficient  $\mu_e$  is given by Beer's law:

$$T = 10^{-\mu_e L} \quad (1)$$

We have purposely used the base 10 formulation here as most UV-Vis spectrometers also use base 10 in their absorbance calculations. The absorbance ( $\mu_e L$ ) from a UV-Vis spectrometer is often mistakenly inferred as absorption, however, it is extinction and is composed of the absorption ( $\mu_a$ ) and scattering ( $\mu_s$ ) coefficients:

$$\mu_e = \mu_a + \mu_s \quad (2)$$

Since the coefficients depend linearly on the concentration of NPs, a useful concentration independent metric is the efficiency of scattering ( $\Psi_s$ ) and absorption ( $\Psi_a$ ) relative to the extinction:

$$\Psi_s = \frac{\mu_s}{\mu_e} \quad \Psi_a = \frac{\mu_a}{\mu_e} = 1 - \Psi_s \quad (3)$$

The scattering coefficient can be measured using a standard fluorometer in synchronous mode where the excitation and emission wavelengths are set to be equal and scanned through the required wavelength range. Unlike extinction, these scattering measurements are relative measurements and require a special reference material to provide an absolute scale. The reference corrects for the excitation source intensity, detector efficiency and excitation and collection efficiencies of the fluorometer which are all wavelength dependent. A suitable reference material for scattering measurements must have negligible absorption at the wavelengths of interest ( $\Psi_s = 1$ ). NPs made from insulators such as silica or semiconductor NPs with sufficiently wide bandgaps (for example ZnO and TiO<sub>2</sub> at visible/IR wavelengths) satisfy this criterion.

## 2.2 Correcting for inner filter effects

Both the reference and the sample need to be corrected for inner filter effects that are similar to the primary and secondary inner filter effects in conventional fluorescence spectroscopy (see reference [23] for an in-depth discussion on inner filter effects). In RLS, inner filter effects refer to the attenuation of the excitation light before it reaches the sensing volume of the cuvette and attenuation of the scattered light after it leaves the sensing volume. The attenuation occurs through both absorption and scattering from the NPs.

There are a number of methods borrowed from traditional fluorescence spectroscopy that can be used to remove or correct for inner filter effects. The simplest way to remove the inner filter effect is to perform scattering measurements at low concentrations (usually with  $\mu_e < 0.05 \text{ cm}^{-1}$ , known as the dilute concentration limit) where inner filter effects are negligible [23,24]. At these concentrations the observed scattering signal ( $I_{obs}$ ) is given by:

$$I_{obs} = C \mu_s \quad \text{or} \quad \frac{I_{obs}}{\mu_e} = C \Psi_s = \alpha \quad (4)$$

where C is the instrumentation correction factor which is dependent on the wavelength but not the sample. For the reference material,  $\alpha_{ref} = C$  so the scattering efficiency of the sample is simply:

$$\Psi_s = \frac{\alpha_{sample}}{\alpha_{ref}} \quad (5)$$

From  $\Psi_s$  the absorption and scattering coefficients can be calculated using Eqs. (2) and (3) at a chosen concentration.

Since the extinction of NPs often varies strongly with wavelength, this method involves ‘stitching’ together several scattering measurements across different wavelength regions. This can produce quite noisy data due to the dilute nature of the sample, especially when the samples are weakly scattering ( $\Psi_s \ll 1$ ) compared to absorption. It also requires careful dilution practices since extinction measurements must be made at higher concentrations (usually with  $0.1 < \mu_e < 1 \text{ cm}^{-1}$ ) then quantitatively diluted for scattering measurements.

An alternative technique is to use a fluorometer calibration approach so that scattering measurements can be performed at higher sample concentrations [21]. This approach is particularly useful if the sample is concentration sensitive, however, it only works reliably when the sample is weakly scattering compared to the absorption.

Since NP samples can display both high and low levels of scattering, neither of these traditional techniques are appealing for RLS of NPs. To extend the applicability of the dilute concentration technique to higher concentrations ( $\mu_e < 0.5 \text{ cm}^{-1}$ ), we found both theoretically

and experimentally that the observed scattering signal can be adequately approximated by adding an additional term to Eq. (4):

$$\frac{I_{obs}}{\mu_e} = \alpha - B\mu_e \quad (6)$$

Here the value of B is always positive and is mostly due to the inner filter effect but also accounts for the nonlinearity of Beer's law beyond the dilute concentration limit. Experimentally, scattering measurements are performed on the reference and sample of interest at different concentrations ( $0.05 < \mu_e < 0.5 \text{ cm}^{-1}$ ) and a straight line is fit to the plot of  $I/\mu_e$  vs  $\mu_e$  for each wavelength value for both the reference and the sample. The fitted values of  $\alpha$  are used in Eq. (5) to find the  $\Psi_s$  of the sample and the values of B are discarded.

Using this modified technique allows scattering measurements of both weakly and strongly scattering samples. Furthermore, the same sample concentration is used for both extinction measurements and scattering measurements so the sample does not need to be quantitatively diluted for measurements at different concentrations.

A fundamental assumption above is that the value of C is independent of the reference or sample NP size and material. This is only true if the scattered intensity (without inner filter effects) as a fraction of the scattering coefficient is the same for both the reference and the sample for all wavelengths. This condition is only strictly met if the NPs can be considered small compared to the wavelengths investigated. When the NPs investigated are not small then a systematic error in the resulting scattering and absorption coefficients will occur that cannot be removed in the RLS technique.

### 2.3 Angular dependence of RLS measurements

The RLS technique relies on measuring the scattered intensity from NPs at a single angle (usually  $90^\circ$ ) to represent the total scattering summed over all possible angles. As mentioned previously, RLS works well if the particles can be considered small. A simple measure of the relative nanoparticle size is the size parameter:

$$x = \frac{2\pi n_{solvent}}{\lambda} r \quad (7)$$

where  $n_{solvent}$  is the refractive index of the solvent,  $\lambda$  is the wavelength and  $r$  is the radius of the NP (or half the length of the longest dimension for non-spherical NPs). When  $x \ll 1$  the scattered intensity as a function of the scattering angle ( $\theta$ ) from an unpolarised light source is given by:

$$I_{x \ll 1}(\theta) = A(1 + \cos^2 \theta)\mu_s = C\mu_s \quad (8)$$

where A is a constant. When the size parameter increases, the  $\theta$  dependence in Eq. (8) no longer holds and scattering in the forward direction starts to dominate. This is unacceptable in quantitative RLS measurements as the fraction  $I(\theta)/\mu_s$  should be independent of the sample. This can be seen in Fig. 1 where we have used Mie theory [27] to demonstrate this concept for Au NPs at a wavelength of 500 nm. For  $x < 0.5$  the  $1 + \cos^2 \theta$  dependence holds quite well, but for larger particles, forward scattering starts to dominate. In Fig. 1 we also compute the error in using a single angle scattering measurement to measure the scattering coefficient as:

$$\frac{\Delta\mu_s}{\mu_s} = \frac{I(\theta)}{A\mu_s(1 + \cos^2 \theta)} - 1 \quad (9)$$

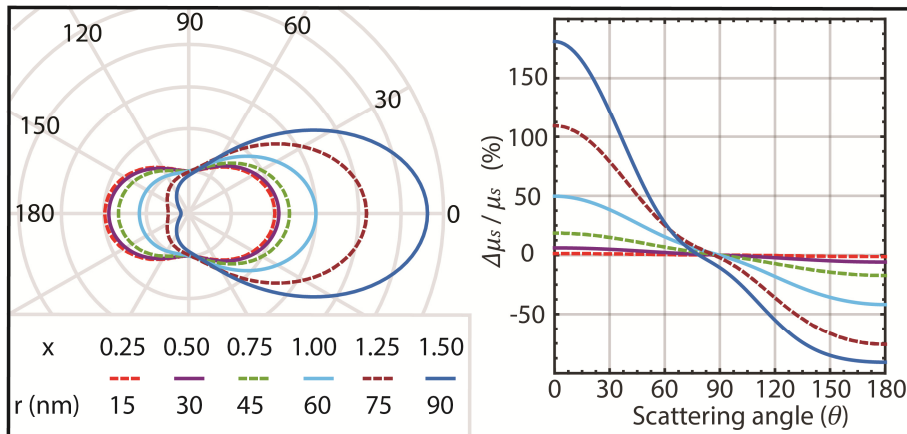


Fig. 1. Simulated scattering polar plot ( $I(\theta) / A\mu_s$ ) for Au NPs (left) and the difference from the small particle approximation (right) for different particle sizes in water at  $\lambda = 500 \text{ nm}$  using Mie theory from [27]. Radial lines in the polar plot have an increment of 1.

Fortunately, the scattering at  $90^\circ$  is the least affected angle by the changing size parameter, making RLS much more accurate than would be expected at other angles. This has never been highlighted before despite how important it is and explains why the experimental reports of RLS on NPs give results that often align well with theory. However, there is still a significant difference in the fraction  $I(90^\circ) / \mu_s$  in larger NPs making separation of absorption and scattering inaccurate. One way to get around the issue of angular dependence of scattering would be to measure the scattering intensity at all angles [26]. Unfortunately, this would not only be time consuming, it is out of reach for the vast majority of researchers who only have access to UV-Vis and fluorometer spectrometers. Figure 1 suggests that if we could do a comparison measurement at another angle, we could check the accuracy of the  $90^\circ$  measurement. Although dip probes are relatively common and work in a  $180^\circ$  backscatter arrangement, they require a larger sample volume, there is a contamination risk and most importantly the signal from large nanoparticles is very weak in the backward direction.

#### 2.4 Scattering measurements at angles other than $90^\circ$

A typical fluorometer operates in a  $90^\circ$  excitation/collection configuration. Here we introduce a simple, fast, and inexpensive modification to a standard fluorometer to perform scattering measurements at angles other than  $90^\circ$  to confirm the accuracy of the  $90^\circ$  scattering measurement. The method involves placing a glass prism in close proximity to the cuvette to redirect the light scattered from the sample (see Fig. 2(d)). Depending on the orientation of the glass prism, this allows scattering measurements in the slightly forward and slightly backward directions.

In order to identify the most appropriate prism angle ( $\phi$ ) to use, we consider the effect of  $\phi$  on the scattering angle ( $\theta$ ) detected, the transmission of the scattered light through the system and the offset of the beam from the center of the cuvette. In order to minimize transmission losses and beam offsets, the prism is positioned as close to the cuvette as possible with the angled side of the prism facing the detector regardless of whether forward or backward scattering is performed. Figure 2(a) and 2(b) shows the scattering angle for the forward and backward configuration and the light transmission through the optical system assuming a 10 mm PMMA cuvette is used. The change in scattering angle ( $90^\circ - \theta$ ) has the same magnitude in either the forward or backward direction and varies approximately linearly with the prism angle. The transmission is the same for both prism configurations and depends on the polarization of the scattered light. The transmission is not ideal above  $30^\circ$  but acceptable as there would still be sufficient signal up to  $60^\circ$ . However, the beam offset (Fig.

2(c)) is unacceptable by  $45^\circ$  assuming a cuvette to prism distance of 4 mm. In this case, without moving the location of the cuvette, the centre of the signal would come from outside a 10 mm cuvette and there would be very little scattering signal at the detector. This suggests the largest prism angle that could be used without moving the location of the cuvette is about  $30^\circ$ . A 30-60-90 prism (also known as a Littrow prism) can perform this function and is readily available from optical component suppliers.

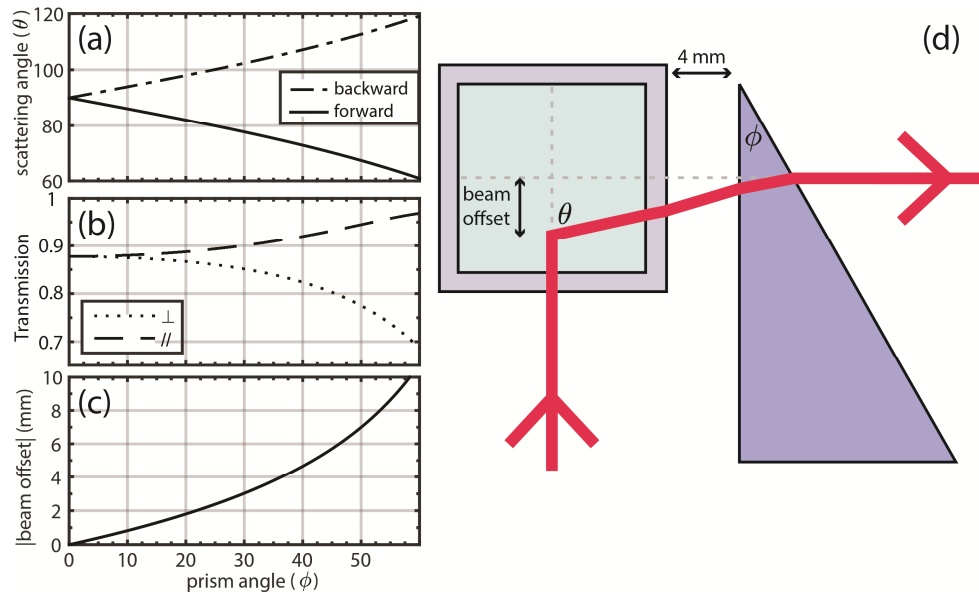


Fig. 2. Utilizing a glass prism to beam steer scattered light. (a) Scattering angle ( $\theta$ ), (b) optical transmission through the system for perpendicular and parallel polarizations, (c) magnitude of beam offset from the centre of the cuvette as a function of the prism angle ( $\phi$ ), (d) schematic of setup (pictured in the forward configuration). Calculations are based on using water as the solvent, 10 mm PMMA cuvette, cuvette to prism distance of 4 mm, BK7 glass prism and  $\lambda = 500 \text{ nm}$ .

### 3. Implementation of RLS

First the reference materials are characterized to ensure that they don't induce any systematic error through unacceptably large particle sizes. We investigate two different commercially available reference materials, colloidal silica (silica-ref) and ZnO NPs (ZnO-ref). To demonstrate how scattering data can be interpreted with the aid of the forward scattering measurements we look at two different types of samples: a semiconductor (80 nm ZnO nanobullets) near the optical bandgap in the UV-visible, and plasmonic NPs (20-200 nm spherical Au NPs) in the visible-NIR. We consider scattering coefficient measurements in the traditional  $90^\circ$  arrangement ( $\mu_{s,90}$ ) and with a Littrow prism as pictured in Fig. 2(d) to give a measurement in the slightly forward direction ( $\mu_{s,\text{for}}$ ). By comparing  $\mu_{s,90}$  and  $\mu_{s,\text{for}}$  the error in  $\mu_{s,90}$  can be estimated.

#### 3.1 Silica and ZnO as reference materials

The ideal reference material would be non-absorbing and have an  $x \ll 1$  for all wavelengths considered. Unfortunately, since the scattered intensity per NP scales with  $r^6$  (for  $x \ll 1$ ) there is insufficient light scattered by very small nanoparticles even at very high concentrations. This requires us to use reference materials that still have zero absorption but of larger size than ideal, i.e.  $x < 1$ . As mentioned previously, colloidal silica is the most

popular choice as a reference material as it has negligible absorption down to wavelengths approaching 250 nm. However, due to its low refractive index contrast with common solvents ( $\sim 0.1$ ), it is difficult to use at wavelengths longer than 500 nm since the scattering signal and extinction coefficient is too low. At these wavelengths it is difficult to source colloidal silica with particle sizes large enough and at high concentrations to scatter sufficient light without resorting to particles with  $x > 1$ . Although ZnO has strong absorption in the UV, it has negligible absorption above 400 nm. Compared to silica, ZnO has a much larger refractive index contrast with most solvents ( $\sim 0.5$ ) which makes it a more suitable reference material in the visible to NIR. We therefore use colloidal silica (Ludox TM-40) and a zinc oxide dispersion (NanoSunguard) as reference materials in the UV-500 nm and 450-850 nm wavelength regions respectively. Both reference materials (silica-ref and ZnO-ref) were purchased from Sigma. Before using in scattering measurements, the materials were diluted in water to 5 wt. % and filtered through a 0.45  $\mu\text{m}$  syringe filter.

Since we have relaxed the size limitation of the reference materials, an error analysis of  $\alpha_{ref}$  was performed in both scattering measurement directions to determine the effect the larger reference NPs have on the measurement of  $\Psi_s$  for the samples described in sections 3.2 and 3.3. The error analysis performed has three steps: (i) measure the reference materials particle size distribution (PSD), (ii) check the accuracy of the PSD using Mie theory and experimental extinction data, (iii) use Mie theory to calculate the theoretical error in measuring  $\alpha_{ref}$  for both scattering angles.

The PSD of the reference materials was found using Dynamic Light Scattering (DLS) in a 173° backscatter arrangement, the intensity weighted PSD are shown in Fig. 3(a). The silica-ref consists of relatively small NPs with more than 99% (intensity weighted) of the NPs with an  $x < 1$  at  $\lambda = 340 \text{ nm}$  whilst the ZnO-ref sample contains larger NPs with 90% (intensity weighted) of the NPs with an  $x < 1$  at  $\lambda = 450 \text{ nm}$ . Although the ZnO-ref does contain unwanted larger NPs, it is still a better reference material than silica-ref in the visible-NIR as we found that the errors incurred from the larger NPs in ZnO-ref are much less than the noise incurred from using silica-ref with an insufficient scattering coefficient.

Using the number weighted PSD from DLS, Mie theory was used to predict the extinction spectra of the reference samples and compared to the measured extinction spectra to determine the accuracy of the measured PSD. Both the theoretical and the experimental spectra were normalized by their mean values to allow comparisons between the theoretical scattering cross-section and the experimental extinction coefficient. The relative difference between the experimental ( $\mu_{e \text{ exp}}$ ) and theoretical ( $\mu_{e \text{ theory}}$ ) extinction data is shown in Fig. 3(b) calculated as:

$$\text{error} = \mu_{e \text{ exp}} / \mu_{e \text{ theory}} - 1 \quad (10)$$

For the silica-ref,  $\mu_{e \text{ theory}}$  overestimates  $\mu_{e \text{ exp}}$  for increasing wavelengths. For ZnO-ref,  $\mu_{e \text{ theory}}$  slightly underestimates  $\mu_{e \text{ exp}}$  for increasing wavelengths. Since large NPs tend to flatten the extinction spectra of non-absorbing NPs, these results indicate that the average particle size from DLS is slightly overestimated for silica-ref and underestimated for ZnO-ref.

The measured PSD was used to calculate the theoretical error in using silica-ref and ZnO-ref as reference materials. The theoretical error in measuring  $\alpha_{ref}$  is shown in Fig. 3(b) for silica-ref and ZnO-ref for both the 90° ( $\alpha_{ref \text{ } 90}$ ) and forward ( $\alpha_{ref \text{ for}}$ ) direction. The error is calculated using Eq. (9) with  $I$  and  $\mu_s$  calculated using the measured PSD and Mie theory. The 90° and forward scattering are slightly under and overestimated respectively with the 90° arrangement being more accurate. This is expected for non-absorbing nanoparticles in this size regime.

For silica-ref, the calculated error is very low and therefore the errors in  $\alpha_{ref\ 90}$  and  $\alpha_{ref\ for}$  can be considered negligible. Since the PSD used was likely slightly overestimated for silica-ref, this also represents an upper limit of the error in  $\alpha_{ref\ 90}$  and  $\alpha_{ref\ for}$  for silica-ref.

For ZnO-ref, the error in  $\alpha_{ref\ 90}$  is still relatively small but the error in  $\alpha_{ref\ for}$  is significant. To compensate for this, the experimental values of  $\alpha_{ref\ for}$  for ZnO-ref (used in section 3.3) were corrected for this deviation. In comparison with silica-ref, the error calculated here is lower limit since the PSD used was likely slightly smaller than the actual distribution. This is important to keep in mind for interpreting the difference between  $\mu_{s\ 90}$  and  $\mu_{s\ for}$  for the Au nanoparticle samples which use ZnO-ref as a reference material.

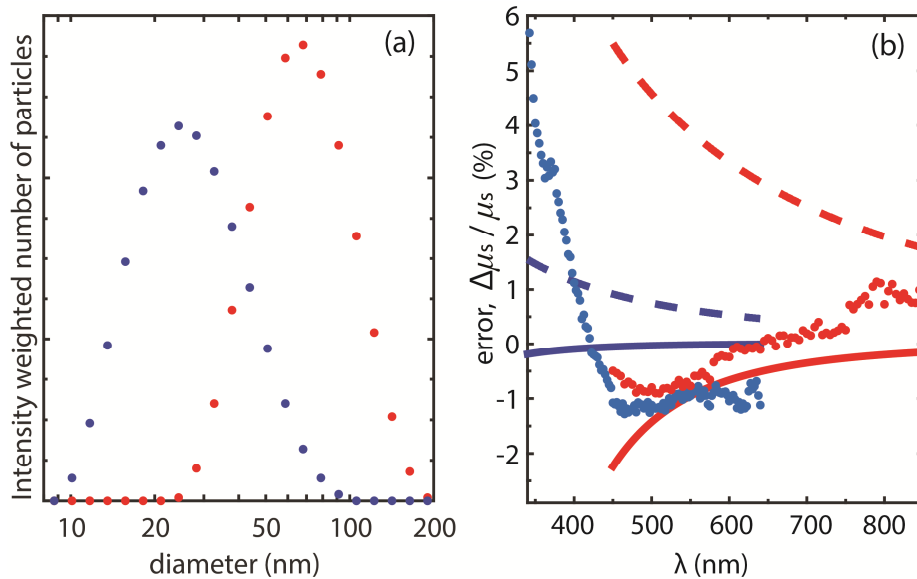


Fig. 3. Reference materials silica-ref (blue) and ZnO-ref (red). (a) DLS intensity weighted particle size distributions. (b) Scattering properties. Dots are the relative difference between experimental extinction data and extinction predicted using the DLS distributions and Mie theory. Solid and dashed lines are the theoretical reference measurement error in measuring the scattering intensity at  $90^\circ$  and the forward direction respectively.

### 3.2 ZnO semiconductor nanobullets

We first look at ZnO nanobullets as a simple example of the technique for a semiconductor material near the optical bandgap of the material using the silica-ref as the reference material. The ZnO nanobullets are approximately 80 nm in size (from transmission electron microscopy (TEM) images) and are dispersed in ethanol. They were synthesized using [28] without using any capping ligands.

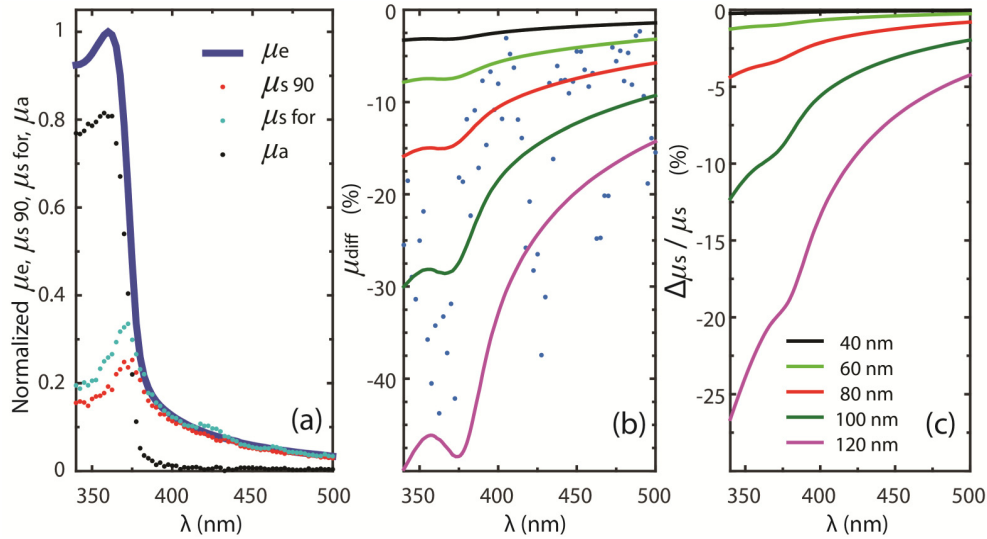


Fig. 4. (a) Measured extinction, scattering and absorption coefficients for ZnO nanobullets. (b) Dots are the relative difference between the two scattering measurements. The solid lines are the theoretical difference for different sized monodisperse ZnO nanospheres calculated using Mie theory. (c) Theoretical error in the 90° scattering measurement for the same nanospheres.

The measured  $\mu_e$ ,  $\mu_{s90}$  and  $\mu_{s\text{for}}$  for the ZnO nanobullets are shown in Fig. 4(a). The  $\mu_a$  calculated using  $\mu_s = \mu_{s90}$  and Eq. (2) is also plotted and agrees well with the optical properties of bulk ZnO. ZnO is a direct bandgap material with an absorption edge near 370 nm and an Urbach tail [29] up until 400 nm. To gauge the accuracy of using  $\mu_s = \mu_{s90}$ , we can look at the difference between the measured  $\mu_{s90}$  and  $\mu_{s\text{for}}$  (Fig. 4(b)) calculated as:

$$\mu_{\text{diff}} = \frac{(\mu_{s90} - \mu_{s\text{for}})}{\mu_{s90}} \quad (11)$$

Although the scattering data is inherently noisy, there is a distinct difference between the measured  $\mu_{s90}$  and  $\mu_{s\text{for}}$ . Since  $\alpha_{\text{ref}}$  has negligible error associated with it for this case,  $\mu_{\text{diff}}$  is due entirely from the scattering measurement of  $\alpha_{\text{sample}}$ . The theoretical  $\mu_{\text{diff}}$  from differently sized monodisperse ZnO nanospheres is also shown in Fig. 4(b). The experimental data fits within the theoretical plots for sizes between 80 and 120 nm. This is to be expected as the largest NPs in the particle size distribution dominate the scattering spectra. The theoretical error in  $\mu_s = \mu_{s90}$  (using Eq. (9)) for differently sized monodisperse ZnO nanospheres is also plotted in Fig. 4(c). This shows that the magnitude of the error in the measured  $\mu_s$  is always less than 25%, but more importantly, the true value of  $\mu_s$  is always somewhere in between  $\mu_{s90}$  and  $\mu_{s\text{for}}$  but closer to  $\mu_{s90}$  for ZnO nanoparticle sizes up to 120 nm. Without  $\mu_{\text{diff}}$ , it would be difficult to know the accuracy of the measured  $\mu_s$  since using the TEM particle size of 80 nm would underestimate the magnitude of the error.

### 3.3 Spherical Au NPs in the visible-NIR

Spherical Au NPs dispersed in water of various diameters were purchased from Nanocomposix (20, 60, 80 and 100 nm) and Sigma (150 and 200 nm). TEM images from the manufacturers confirmed the approximate size of the nanoparticles. The measured  $\mu_e$ ,

$\mu_{s\ 90}$  and  $\mu_{s\ for}$  for the Au NPs are shown in Fig. 5. The scattering spectra of the 20 nm was less than the dark noise level (not included) confirming that for the 20 nm NPs, the scattering component of  $\mu_e$  is negligible and  $\mu_a \sim \mu_e$ . As expected, the scattering component of  $\mu_e$  increases with particle size until the 200 nm NPs where the scattering peak broadens and loses its shape.

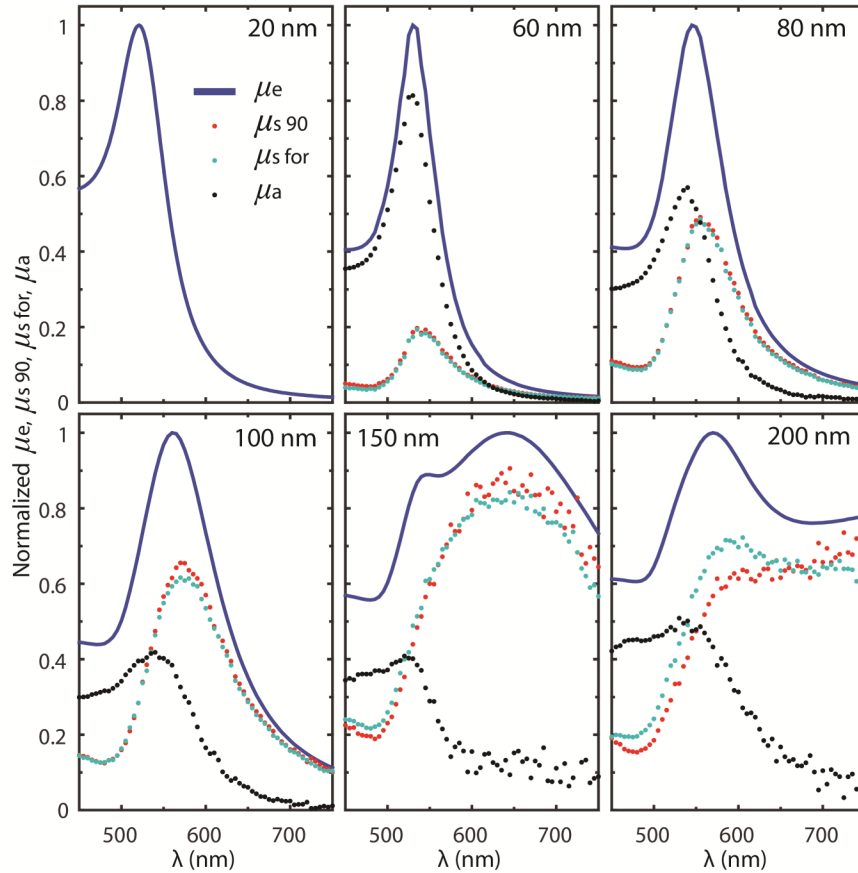


Fig. 5. Measured spectra of Au NPs in water. Nominal Au NP diameter is shown in the corner of each figure. Each spectrum is normalized by the maximum extinction value.

The measured  $\mu_{diff}$  for the Au NP samples with appreciable scattering is shown in Fig. 6(a). The theoretical  $\mu_{diff}$ , assuming monodisperse spherical Au NPs of the same nominal sizes, is shown in Fig. 6(b). Although the overall shapes of the difference spectra are similar between the measured and theoretical spectra, there is a positive offset most obvious in the smallest NPs where theoretically  $\mu_{diff} \sim 0$ . In comparison with the ZnO nanobullets, the measurements here used the ZnO-ref which has a larger size parameter over the wavelengths measured compared to the silica-ref. This results in an appreciable difference between the measured  $\mu_{s\ 90}$  and  $\mu_{s\ for}$  due to ZnO-ref alone despite the attempted correction for  $\alpha_{ref\ for}$ .

The theoretical error in  $\mu_s = \mu_{s\ 90}$  for the Au NPs is shown in Fig. 6(c). Unlike the semiconductor near the bandgap example of ZnO nanobullets, the plasmon resonance in Au makes the correlation between  $\mu_{diff}$  and the error in  $\mu_s$  as a function of wavelength much more difficult. For NP sizes up to 100 nm, there is negligible error in  $\mu_s$  which is well

represented by  $\mu_{diff}$ . Above 100 nm, the magnitude or sign of  $\mu_{diff}$  no longer represents the error in  $\mu_s$  at each wavelength value. To be conservative, we suggest looking at the most extreme values in  $\mu_{diff}$  to indicate the likely magnitude of the error in  $\mu_s$  across the whole spectrum for plasmonic NPs.

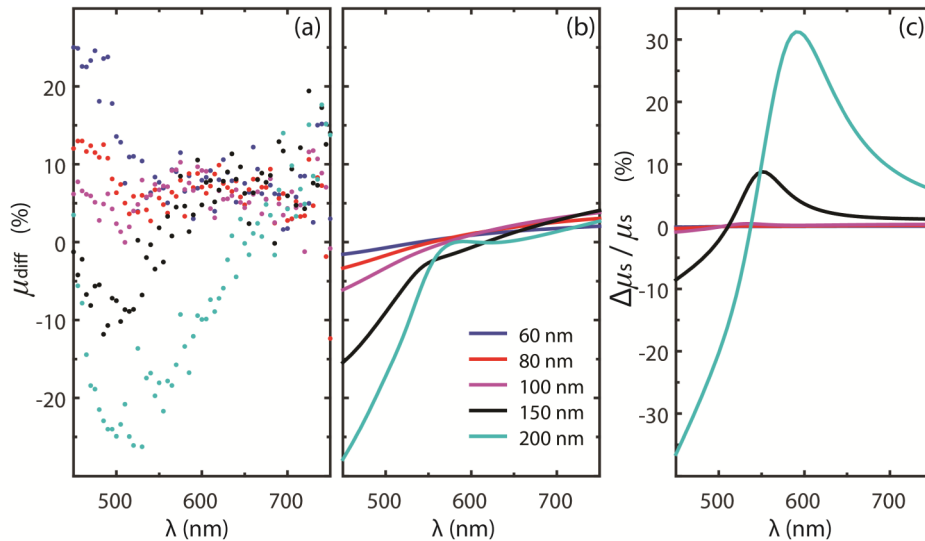


Fig. 6. (a) Difference between the scattering coefficients for the different particle sizes (a) measured (b) theoretical. (c) Theoretical error in 90° scattering measurement. Legend colors in (b) apply to all 3 figures and refer to the nominal Au NP diameter from the NP supplier.

#### 4. Conclusions and outlook

In this paper, we have removed the ambiguities in the RLS technique and detailed the required steps for an accurate measurement of the scattering and absorption coefficients of a NP dispersion. Detailed analysis of the reference material which is rarely performed in previous studies, is required to guarantee the accuracy of the instrumentation correction factor. Since the size parameter is a function of wavelength, one single reference material can't be used across the entire UV-visible-NIR spectrum. For the UV, colloidal silica was found to work very well as a reference material with an adequate scattering coefficient up to a wavelength of 450 nm. In the visible-NIR, an inexpensive dispersion of ZnO was found to work better due to the higher refractive index of ZnO. However, the particle sizes were slightly larger than ideal inducing a measurable error in the forward scattering data.

The inner filter effect can be compensated for in a straightforward manner by performing measurements at multiple concentrations and extrapolating towards the dilute concentration limit. This allows measurements of scattering and extinction at the same concentrations, eliminating the need for highly accurate dilution practices.

We have also shown a very simple and straightforward adaption of a standard fluorometer using an inexpensive glass prism to perform RLS in either the slightly forward or backward direction. This secondary measurement allows the accuracy of the measured scattering coefficient to be gauged.

Using the RLS technique, the bandgap of ZnO nanobullets was confirmed to be approximately 370 nm with little to no absorption above a wavelength of 400 nm. For semiconductor materials, the difference spectra ( $\mu_{diff}$ ) allows the accuracy of the absorption/scattering spectra to be estimated. This is particularly important for semiconductors with unknown optical properties such as doped or alloy semiconductors since

there will be no way to accurately model the absorption spectra even if the particle size distribution is well known.

For Au NPs, the extinction spectra were separated into absorption and scattering components. Although  $\mu_{diff}$  could not be used to estimate the error in  $\mu_s$  for the largest Au NPs at each wavelength, using the extreme values of  $\mu_{diff}$  indicated the reliability of the measured  $\mu_s$ . Similar to semiconductor NPs, metal alloy NPs will greatly benefit from this technique as the optical properties of metallic alloys are often unknown.

The broad applicability of the RLS method still needs to be explored for other particle shapes and hybrid NPs. Hybrid materials are of particular interest as they usually cannot be modelled accurately due to both the complex geometry of the NP and the variability within a dispersion. A good example is large metal oxide semiconductor NPs decorated in smaller metallic NPs [28,30] that are widely used in visible light photocatalysis applications. Understanding the amount of visible light absorption by the metallic NP within the large scattering background would greatly help understand the mechanism of electron/hole transfer and guide design of more efficient hybrid NPs for photocatalysis.

Another important application of the RLS technique is in situ measurements of absorption and scattering coefficients during a chemical reaction or particle aggregation event. These types of phenomena are inherently dependent on the concentration of the NPs in the solution so removing the inner filter effect by extrapolating towards the dilute concentration limit is not possible for in situ measurements. It should be possible to use the value of  $B$  in Eq. (6) from the reference material to calculate  $\alpha_{sample}$ . However, more work needs to be done to understand how  $B$  is effected by the NP size parameter and  $\Psi_s$  since scattering (particularly forward scattering) will not produce an inner filter effect as large as absorption will.

### Funding

Air Force Research Laboratory (FA2386-14-1-4056).

### Acknowledgments

Microscopy and DLS was carried out at the Central Analytical Research Facility, IFE. M.P.S gratefully acknowledges Monique Tourell for her assistance in manuscript preparation and Kazuyuki Hosokawa for his technical assistance.